

Weyl points of mechanical diamond

Yuta Takahashi^{1,*}, Toshikazu Kariyado^{2,†} and Yasuhiro Hatsugai^{3‡}

¹*Graduate School of Pure and Applied Science, University of Tsukuba, Tsukuba, Ibaraki 305-8571, Japan*

²*International Center for Materials Nanoarchitectonics(WPI-MANA),*

National Institute for Materials Science, Tsukuba, Ibaraki 305-0044, Japan

³*Division of Physics, University of Tsukuba, Tsukuba, Ibaraki 305-8571, Japan*

(Dated: January 15, 2019)

A spring-mass model arranged in a diamond structure — mechanical diamond — is analyzed in terms of topology in detail. We find that, additional springs connecting the next-nearest-neighbor pairs of mass points and the modulation of the mass parameters to the pristine mechanical diamond generates multiple pairs of Weyl points in the frequency dispersion. Evolution of the Weyl point positions in the Brillouin zone against the uniform outward tension is tracked and explained by the point group symmetry, especially tetrahedral symmetry of the NNN springs. Interestingly, there happens a rapid transmutation of the monopole charges of the Weyl points as the tension varies. We also show surface Fermi arcs in the case with anisotropy in the NNN springs.

I. INTRODUCTION

Topological semimetals, which are characterized by isolated gapless points or lines in their band structure, have been intensively studied both in theoretical and experimental view points recently. There are two classes of topological semimetals: one requires some symmetry for protection of the gapless points, while the other is purely topological. The former includes Dirac semimetals with time reversal and spatial inversion symmetries, or nodal line semimetals that are protected by reflection symmetry, for instance¹⁻⁷. On the other hand, the latter includes Weyl semimetals where either of time reversal or spatial inversion symmetry is required to be broken⁸⁻¹³. Namely, for the Weyl semimetals, symmetry breaking is the key for generating gapless points (Weyl points). The Weyl points are created/annihilated as pairs and each of a pair carries ± 1 topological charge, and the conservation of the topological (or monopole) charge is behind the stability of the Weyl points. The topological nature of the Weyl points are also reflected in surface states: a Weyl semimetal is characterized by a Fermi arc, which is an isoenergy line of the surface state at the Fermi energy connecting a pair of Weyl points projected onto the surface Brillouin zone^{14,15}. We can relate the surface Fermi arc with the bulk Chern number, forming a typical example of bulk-edge correspondence¹⁶.

Currently, the concept of topological insulators/semimetals and bulk-edge correspondence is extended to wider and wider variety of systems including classical systems such as photonic crystals^{17,18} and mechanical systems¹⁹⁻²⁵. It is possible to mimic quantum Hall states, quantum spin Hall states, and other topologically nontrivial states by appropriate artificial designs. Roughly speaking, the typical design goes as follows. In a spatially periodic classical system, the frequency-wavenumber dispersion relation of the normal modes forms a band structure, just like the energy-momentum dispersion relations in quantum solids. Then, we choose structures and parameters so as to make the band structure of the normal modes

resembling to the band structure of topological insulators/semimetals. The designed nature is an advantage of the classical topological systems over the quantum electronic systems. Namely, the classical systems usually have better controllability than the quantum ones, and enables us to access parameter regions that are impossible or difficult in experiments in quantum systems. Mechanical graphene, a spring-mass model with the honeycomb structure having Dirac cones in its frequency dispersion, enjoys this controllable feature²⁶⁻²⁸. For instance, the number and positions of the Dirac cones can be changed simply by a uniform outward tension. If the Dirac cones are gapped out by a time-reversal symmetry breaking term, there appear chiral edge mode, and the uniform outward tension causes a flip in the flowing direction of the chiral edge mode. Mechanical graphene has a natural extension in three-dimension, i.e., mechanical diamond that is a spring-mass model with diamond structure²⁹. We have found that mechanical diamond is a classical counterpart of the nodal line semimetal, i.e., having lines of degeneracy in the frequency dispersion, and a (modified) chiral symmetry is the key for line node protection²⁹.

In this paper, we investigate symmetry breaking effects on the frequency-wavenumber dispersion relation of the normal vibration modes in the mechanical diamond. The (modified) chiral symmetry is broken by introducing springs connecting next-nearest-neighbor (NNN) pairs of mass points in addition to the original ones for the nearest neighbor (NN) pairs, and introducing modulation in mass of the mass points. This symmetry breaking eliminates the line nodes and generates several Weyl points. It is noticed that the tetrahedral symmetry of the system is crucial in determining the number of the Weyl points. As in the case of mechanical graphene, the uniform outward tension induces movement of the Weyl points along the line originally being line nodes. Interestingly, an exchange of chirality (or topological charge) occurs as the Weyl points travel about. We also investigate surface states to see Fermi arcs associated with the nontrivial topology in the bulk with Weyl points.

In the following, we start with describing two types of the mechanical diamond, a NN model and a NNN model in Sec. II. Section III is for numerical methods to identify Weyl points. Mappings of the Weyl points for an isotropic case and an anisotropic case are shown in Sec. IV, and the results are interpreted in terms of symmetry. Section V considers Fermi arcs for the anisotropic case in a system with a boundary. The paper is concluded in Sec. VI.

II. MODEL

A. Nearest-neighbor (NN) model

A mechanical diamond is a classical model composed of mass points and springs arranged in a diamond structure. We first consider NN model, where the springs connect the neighboring pairs of the mass points. The parameters describing our model are spring constant of the NN springs κ , mass of the mass points m , natural length of the NN springs l_0 and distance between the neighboring mass points R_0 . If we apply uniform outward tension, the distance R_0 can be larger than the natural length l_0 . This deformation is enabled by a proper boundary condition. One possible way to exert the outward tension is to hang the entire system into some cage, and to apply the fixed boundary condition by connecting the outer most mass points to the cage. For simplicity, m is set to unity in this NN model. The dynamical variables of the model are $\mathbf{x}_{\mathbf{R}a} = (x_{\mathbf{R}a}, y_{\mathbf{R}a}, z_{\mathbf{R}a})$, which are displacements of mass points from the equilibrium positions with \mathbf{R} denoting the lattice points and a being a sublattice index. In the following, we focus on infinitesimal oscillation about the equilibrium positions, and $\mathbf{x}_{\mathbf{R}a}$ is regarded as a small quantity.

The elastic energy of a single linear spring U_s is approximated as $U_s \simeq U_0 + U_1(\delta x_\lambda) + U_2(\delta x_\mu \delta x_\nu)$, with $\delta \mathbf{x}$ indicating a difference between the displacements of the neighboring pair of the mass points. The U_1 -term that is first order in δx_λ can be finite for a single spring, but if we consider all the springs connected to a single mass point, the terms cancel out with each other. Then, the dynamics of the system is governed by the U_2 -term that is second order in δx_λ . The U_2 -term is explicitly written as

$$U_2(\delta x_\mu \delta x_\nu) = \frac{1}{2} \kappa \delta x_\mu \gamma_{\mathbf{R}_0}^{\mu\nu} \delta x_\nu, \quad (1)$$

where $\gamma_{\mathbf{R}_0}^{\mu\nu} = (1 - \eta) \delta^{\mu\nu} + \eta \hat{R}_0^\mu \hat{R}_0^\nu$, $\hat{\mathbf{R}}_0 = \mathbf{R}_0 / |\mathbf{R}_0|$ and $\eta \equiv l_0 / R_0$. The summation over μ and ν , which run

through three spatial directions (x, y, z), is implicitly taken. Importantly, the tension parameter η determines the U_2 -term.

Substituting four NN vectors $\mathbf{R}_0^{(i)}$ ($i = 1, 2, 3, 4$) into $U_2(\delta x_\mu \delta x_\nu)$, and applying Fourier transformation in time and space, i.e., using $\mathbf{x}_{\mathbf{R}a} = \frac{1}{N} \sum_{\mathbf{k}} e^{i(\mathbf{k} \cdot \mathbf{R} + \omega t)} \phi_{\mathbf{k}a}$, the Newton's equation of motion becomes

$$\hat{\Gamma}(\mathbf{k}) \phi(\mathbf{k}) = \omega^2 \phi(\mathbf{k}), \quad (2)$$

where

$$\hat{\Gamma}(\mathbf{k}) = 4\kappa(1 - \frac{2}{3}\eta) \hat{1} + \begin{pmatrix} \hat{0} & \hat{\Gamma}_{AB}(\mathbf{k}) \\ \hat{\Gamma}_{AB}^\dagger(\mathbf{k}) & \hat{0} \end{pmatrix}, \quad (3)$$

and $\hat{\Gamma}_{AB}(\mathbf{k}) = -\kappa(\hat{\gamma}_4 + e^{-i\mathbf{k} \cdot \mathbf{a}_1} \hat{\gamma}_1 + e^{-i\mathbf{k} \cdot \mathbf{a}_2} \hat{\gamma}_2 + e^{-i\mathbf{k} \cdot \mathbf{a}_3} \hat{\gamma}_3)$, with $\hat{\gamma}_i \equiv \hat{\gamma}_{\mathbf{R}_0^{(i)}}$ ($i = 1, 2, 3, 4$). A frequency dispersion is obtained from this secular equation. Note that $\hat{\Gamma}(\mathbf{k})$ has a chiral symmetry if the diagonal terms are subtracted, i.e., $\hat{\Gamma}'(\mathbf{k}) = \hat{\Gamma}(\mathbf{k}) - 4\kappa(1 - \frac{2}{3}\eta)$ anticommutes with $\hat{\Upsilon} = \text{diag}(1, 1, 1, -1, -1, -1)$. As discussed in Ref. 29, by making use of the Berry's parameterization of a two band effective model near a gap closing point, it can be shown that the gap closing point should form a line (line node) in the 3D Brillouin zone³⁰ with the chiral symmetry. In contrast, the gap closing point becomes an isolated point (Weyl point) in the 3D Brillouin zone without chiral symmetry. In the following, we consider to add a term breaking the chiral symmetry in mechanical diamond.

B. Next-nearest-neighbor (NNN) model

In order to break the chiral symmetry, we introduce (i) springs connecting the next-nearest-neighbor pairs of the mass points on one of the sublattices only (say, the sublattice A out of the sublattices A and B) (see Fig. 1), and (ii) difference in the mass of the mass points between the two sublattices by writing the mass for the sublattice A as m while keeping the mass for the sublattice B to be 1. Following the arguments in the previous subsection, and using six NNN vectors $\mathbf{R}_1^{(i)}$ ($i = 1, 2, \dots, 6$) in Fig. 1, the secular equation to be solved becomes

$$\hat{\Gamma}_{NNN}(\mathbf{k}) \phi'(\mathbf{k}) = \omega^2 \phi'(\mathbf{k}), \quad (4)$$

with

$$\hat{\Gamma}_{NNN}(\mathbf{k}) = \begin{pmatrix} \hat{\Gamma}_{AA}(\mathbf{k})/m & \hat{\Gamma}_{AB}(\mathbf{k})/\sqrt{m} \\ \hat{\Gamma}_{AB}^\dagger(\mathbf{k})/\sqrt{m} & \hat{\Gamma}_{BB} \end{pmatrix}. \quad (5)$$

Here,

$$\begin{aligned} \hat{\Gamma}_{AA}(\mathbf{k}) = & \hat{\Gamma}_{BB} + 2\kappa'_1[1 - \cos(\mathbf{k} \cdot \mathbf{a}_1)]\hat{\gamma}'_1 + 2\kappa'_2[1 - \cos(\mathbf{k} \cdot \mathbf{a}_2)]\hat{\gamma}'_2 + 2\kappa'_3[1 - \cos(\mathbf{k} \cdot \mathbf{a}_3)]\hat{\gamma}'_3 \\ & + 2\kappa'_4[1 - \cos(\mathbf{k} \cdot (\mathbf{a}_1 - \mathbf{a}_2))]\hat{\gamma}'_4 + 2\kappa'_5[1 - \cos(\mathbf{k} \cdot (\mathbf{a}_2 - \mathbf{a}_3))]\hat{\gamma}'_5 + 2\kappa'_6[1 - \cos(\mathbf{k} \cdot (\mathbf{a}_3 - \mathbf{a}_1))]\hat{\gamma}'_6, \end{aligned} \quad (6)$$

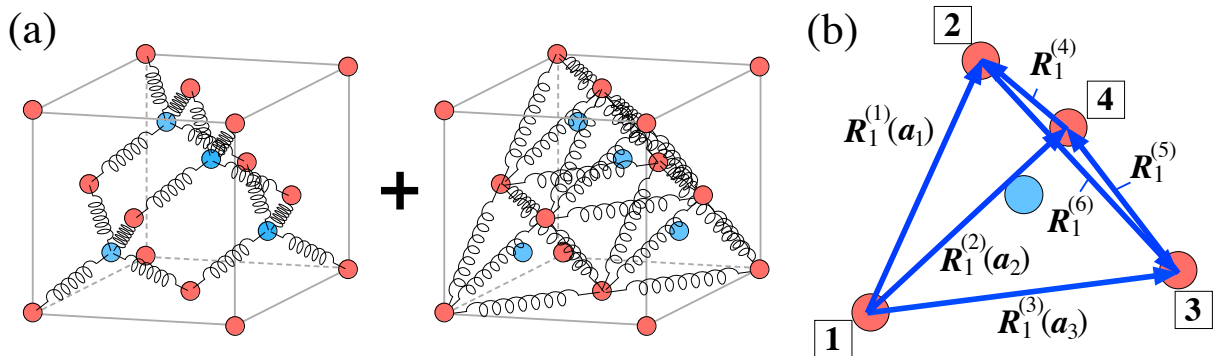


FIG. 1. (a) Schematic picture of the NNN model. Red (blue) mass points are labeled as sublattice A (B). (b) Definitions of NNN vectors $\mathbf{R}_1^{(i)}$. In particular, the three vectors $\mathbf{R}_1^{(1)}$ - $\mathbf{R}_1^{(3)}$ are exactly the same as the unit translation vectors \mathbf{a}_1 - \mathbf{a}_3 respectively. The four vertices of a tetrahedron formed by the NNN springs are numbered (from 1 to 4) to discuss a symmetry in §IV.

with $\hat{\gamma}'_i \equiv \hat{\gamma}_{\mathbf{R}_1^{(i)}} = (1 - \eta')\delta^{\mu\nu} + \eta'\hat{R}_1^{(i)\mu}\hat{R}_1^{(i)\nu}$, $\hat{\mathbf{R}}_1 = \mathbf{R}_1/|\mathbf{R}_1|$, $\hat{\Gamma}_{BB} = 4\kappa(1 - \frac{2}{3}\eta)\hat{1}$ and $\hat{\Gamma}_{AB}(\mathbf{k})$ is unchanged from the previous subsection. The new tension parameter η' is defined as $\eta' \equiv l_1/R_1$ where l_1 is natural length of the NNN springs and $R_1 = |\mathbf{R}_1|$. A uniform and isotropic outward tension preserves the ratio between R_0 and R_1 , and therefore, we have $\eta' = \frac{\eta'_0}{\eta_0}\eta$ where η_0 and η'_0 are the tension parameters of the NN and NNN springs at some reference tension, respectively.

Note that we have assigned different spring constants for NNN springs lying in different directions, i.e., κ'_i ($i = 1, 2, \dots, 6$) for the NNN springs in the $\mathbf{R}_1^{(i)}$ directions. For the NN springs, the forces exerted on a single mass point are balanced between four springs in equilibrium, and it is better to assign the same spring constants for four springs to keep the ideal diamond structure. On the other hand, for the NNN springs, the forces on a mass point are balanced in a pairwise way in each of the six directions along $\mathbf{R}_1^{(i)}$ in equilibrium, and the ideal diamond structure is kept even if we assign different spring constants for different directions³¹. As we have noted, the mass parameters depend on the sublattices, and in that case, a naive treatment makes the problem a generalized eigenvalue problem. However for convenience, we have reformulated it into a standard eigenvalue problem with an hermitian matrix $\hat{\Gamma}_{NNN}(\mathbf{k})$ by absorbing the factor m into the eigenvectors as $\phi'(\mathbf{k}) = \text{diag}(\sqrt{m}, \sqrt{m}, \sqrt{m}, 1, 1, 1)\phi(\mathbf{k})$. In the last subsection, subtraction of the diagonal part proportional to an identity matrix was essential to show that the model obeys a (modified) chiral symmetry. For NNN model, since the block matrix $\hat{\Gamma}_{AA}$ depends on the momentum, it is no longer possible to remove/neglect it in the symmetry argument.

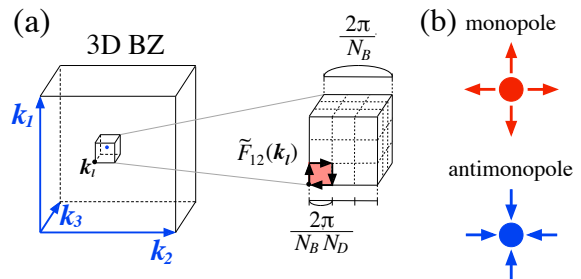


FIG. 2. (a) Schematic picture of the procedure to detect Weyl points. A lattice field strength $\tilde{F}_{12}(\mathbf{k}_l)$ is calculated on the red area as a part of one face of a minicube. (b) Definition of a monopole (antimonopole), with the arrows represent the flow of the Berry flux. The monopole (antimonopole) corresponds to chirality $+$ ($-$).

III. NUMERICAL METHOD

Our major task in the following is to identify Weyl points. In numerics, it is nontrivial to distinguish a strictly gapless point from a tiny but finitely gapped point if we only look at eigenvalue spectra. Therefore, we try to extract more information from eigenstates. Specifically, we numerically locate monopoles in Brillouin zone (Weyl points) by evaluating Berry curvature. Here, the well-established method^{32,33} is adapted for the evaluation of the Berry curvature. Specifically, the procedure is as follows [see also Fig. 2(a)]. First, the Brillouin zone is divided into coarse cubes whose corners are labeled by $\mathbf{k}_l = (k_{l_1}, k_{l_2}, k_{l_3})$ where $\mathbf{l} = (l_1, l_2, l_3)$, $k_{l_\mu} = 2\pi l_\mu/N_B$ and $l_\mu = 0, \dots, N_B - 1$. Then we define a $U(1)$ link variable by

$$U_\mu(\mathbf{k}) \equiv \frac{\det \psi^\dagger(\mathbf{k}) \psi(\mathbf{k} + \hat{\mathbf{e}}_\mu)}{|\det \psi^\dagger(\mathbf{k}) \psi(\mathbf{k} + \hat{\mathbf{e}}_\mu)|}, \quad (7)$$

where $\psi(\mathbf{k})$ is a triplet state of which components are three states with lower frequencies. We have also put in a shorthand notation $\hat{e}_\mu = 2\pi/(N_B N_D)(\delta_{1\mu}, \delta_{2\mu}, \delta_{3\mu})$ with a quantity N_D denoting the number of discretized mesh points on the surface of the coarse cube. For the square spanned by \mathbf{k}_l , $\mathbf{k}_l + \hat{e}_\mu$, $\mathbf{k}_l + \hat{e}_\nu$ and $\mathbf{k}_l + \hat{e}_\mu + \hat{e}_\nu$ ($\mu \neq \nu$),

a lattice field strength is given as

$$\tilde{F}_{\mu\nu}(\mathbf{k}_l) \equiv \text{Arg} \frac{U_\mu(\mathbf{k}_l) U_\nu(\mathbf{k}_l + \hat{e}_\mu)}{U_\mu(\mathbf{k}_l + \hat{e}_\nu) U_\nu(\mathbf{k}_l)},$$

$$-\pi < \tilde{F}_{\mu\nu}(\mathbf{k}_l) \leq \pi, \quad (8)$$

and a monopole charge of one coarse cube \tilde{C}_l is computed from $\tilde{F}_{\mu\nu}(\mathbf{k}_l)$ as

$$\tilde{C}_l = \frac{1}{2\pi} \sum_{i,j=0}^{N_D-1} [-\tilde{F}_{12}(\mathbf{k}_l + i\hat{e}_1 + j\hat{e}_2) - \tilde{F}_{23}(\mathbf{k}_l + i\hat{e}_2 + j\hat{e}_3) - \tilde{F}_{31}(\mathbf{k}_l + i\hat{e}_3 + j\hat{e}_1) + \tilde{F}_{12}(\mathbf{k}_{l+(0,0,1)} + i\hat{e}_1 + j\hat{e}_2) + \tilde{F}_{23}(\mathbf{k}_{l+(1,0,0)} + i\hat{e}_2 + j\hat{e}_3) + \tilde{F}_{31}(\mathbf{k}_{l+(0,1,0)} + i\hat{e}_3 + j\hat{e}_1)]. \quad (9)$$

When this monopole charge results in a nonzero integer, at least one Weyl point exists in that cube. (In general, we have to note that even if this monopole charge is zero, we still have a chance to find multiple Weyl points with compensated charges.) Hence, we pick up cubes with finite monopole charges and repeat this procedure (subdivide into smaller cubes) until we have a solo Weyl point in each cube.

IV. POSITION OF WEYL POINTS

A. Isotropic case

We first see a typical band structure in Fig. 3(a). For $\eta = 0.7$, we see a Weyl point as a band crossing on the X-W line. Here, the crossing is between a flat band and a dispersive band, implying the found Weyl point is marginal in terms of the type I and type II classification. Then, equipped with the method in the previous section, we investigate Weyl points in NNN model of mechanical diamond more in detail. Figures 3(b)-3(e) shows Weyl points for an isotropic case, where $\kappa = 1/(1 - \frac{2}{3}\eta)$, $\kappa'_i = 0.2/(1 - \frac{2}{3}\eta)$ ($i = 1, 2, \dots, 6$), $\eta_0 = 1$, $\eta'_0 = 0.8$ and $m = 2$. We have applied the dividing procedure twice. In the first step, we use $N_B^{1\text{st}} = 41$ and $N_D^{1\text{st}} = 5$, and in the second step, we use $N_B^{2\text{nd}} = 5$ and $N_D^{2\text{nd}} = 3$, in which the length of the edge of the smallest cube is $1/205$ of the Brillouin zone size. A red (blue) point stands for a Weyl point of a monopole (antimonopole) as described in Fig. 2(b). We find six pairs of the Weyl points moving from the W points to the X points as the tension increases, or η decreases. Note that the line node in NN model passes through the line connecting the W and X points. In decreasing η , the Weyl points are created as pairs at the W points, and annihilated with those from the other pairs at the X points.

Remarkably, the colors of the Weyl points are different between Fig. 3(b) and Fig. 3(c), i.e., there is a rapid transmutation of the monopole charge from positive to

negative (or vice versa). This transmutation occurs in between $\eta = 0.67$ and $\eta = 0.66^{34}$. Figure 4 illustrates the detailed process of the transmutation. Because of the three-fold rotational symmetry and the reflection symmetry of the system, it is sufficient to examine one of the square faces of the fcc Brillouin zone. In the rest of this paragraph, we focus on the number of Weyl points only on the one square face. (The total number of generated Weyl points in the entire Brillouin zone is obtained by triplication.) For an illustrative purpose, we put numbers on found Weyl points as in the right panels of Fig. 4. Also as a guidance, we draw line nodes for the corresponding NN model with chiral symmetry in Fig. 4. (There are no line nodes anymore without the chiral symmetry.) As η decreases from 0.6680 to 0.6635, the number of the Weyl points on the square face changes as $4 \rightarrow 12$ (original 4 + new 8) $\rightarrow 4$. For $\eta = 0.6680$, the four Weyl points (No. 1–No. 4) are at the crossing points between the straight and circularlike line nodes. For $\eta = 0.6675$, new eight Weyl points (No. 5–No. 8 and No. 5'–No. 8') are found on the circularlike line node. These new Weyl points are created as pairs of No. 5–No. 6, No. 6'–No. 7', No. 7–No. 8, and No. 8'–No. 5'. For $\eta = 0.6645$, the two pairs of the monopoles No. 5–No. 5' and No. 7–No. 7' approach to the antimonopoles No. 1 and No. 3 along the trace of the circularlike line nodes, respectively. At the same time, the two pairs of the antimonopoles No. 6–No. 6' and No. 8–No. 8' come close to the monopoles No. 2 and No. 4. Finally, only two monopoles and two antimonopoles that have the opposite charges from the $\eta = 0.6680$ case remain at the intersection of the straight and circularlike line nodes for $\eta = 0.6635$.

It is helpful to think of the tetrahedral symmetry of the NNN springs in understanding the number of the Weyl points in the first Brillouin zone. Here, we use the numbers in Fig. 1(b). There are $4! = 24$ symmetric operations to exchange the vertices in the tetrahedron, which are mapped on the permutations of (1,2,3,4) to form the symmetric group S_4 . Out of 24, 12 do not involve the mirror operation (see Fig. 5), forming the alternating sub-

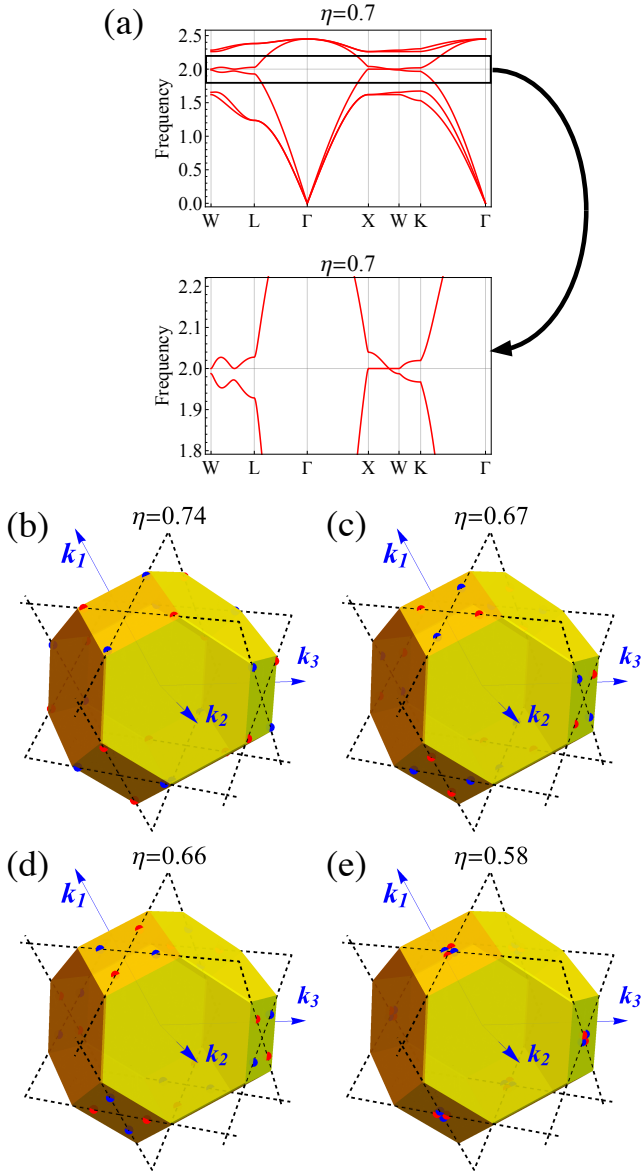


FIG. 3. (a) Bulk band structure for $\eta = 0.7$. We employ the standard notation for the high symmetry points in the fcc Brillouin zone. The third and fourth bands are crossing between the X and W points. (b)-(e) Weyl points for the isotropic case. The tension parameters are (b) $\eta = 0.74$, (c) $\eta = 0.67$, (d) $\eta = 0.66$ and (e) $\eta = 0.58$. The three blue arrows marked with \mathbf{k}_1 , \mathbf{k}_2 and \mathbf{k}_3 are the reciprocal vectors of the diamond lattice. The dashed lines indicate the line nodes in the chiral symmetric case, which are found irrespective of the value of η . (For the chiral symmetric case, there are other line nodes in a certain range of η . See Fig. 4 and Ref. 29.)

group A_4 , whose elements are: $I(1, 2, 3, 4) = (1, 2, 3, 4)$, $V_1(1, 2, 3, 4) = (2, 3, 1, 4)$, $V_1^{-1}(1, 2, 3, 4) = (3, 1, 2, 4)$, $V_2(1, 2, 3, 4) = (1, 3, 4, 2)$, $V_2^{-1}(1, 2, 3, 4) = (1, 4, 2, 3)$, $V_3(1, 2, 3, 4) = (3, 2, 4, 1)$, $V_3^{-1}(1, 2, 3, 4) = (4, 2, 1, 3)$, $V_4(1, 2, 3, 4) = (2, 4, 3, 1)$, $V_4^{-1}(1, 2, 3, 4) = (4, 1, 3, 2)$, $E_1(1, 2, 3, 4) = (2, 1, 4, 3)$, $E_2(1, 2, 3, 4) = (3, 4, 1, 2)$ and

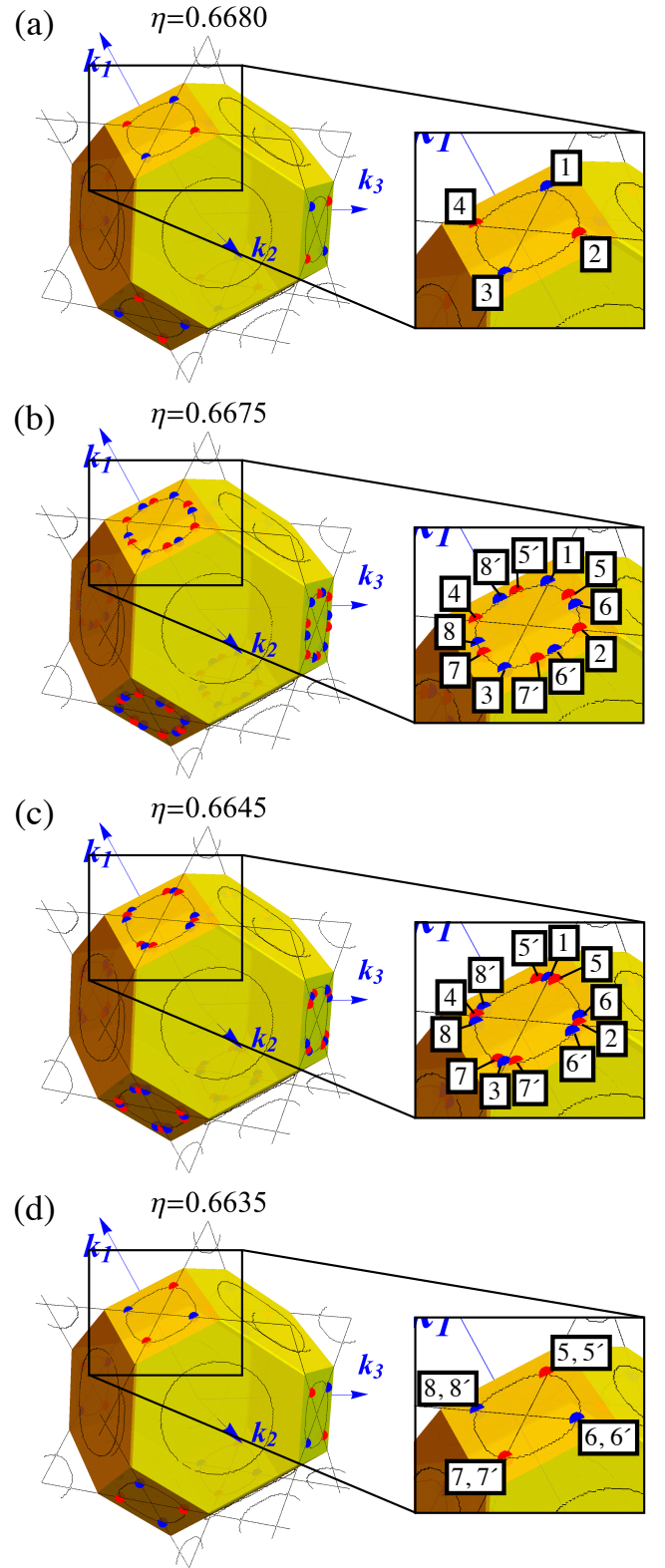


FIG. 4. Details for the switch of the positive and negative chiralities. The tension parameters are (a) $\eta = 0.6680$, (b) $\eta = 0.6675$, (c) $\eta = 0.6645$ and (d) $\eta = 0.6635$. Black lines represent the numerically obtained line nodes in the NN model (i.e., with chiral symmetry) for each η .

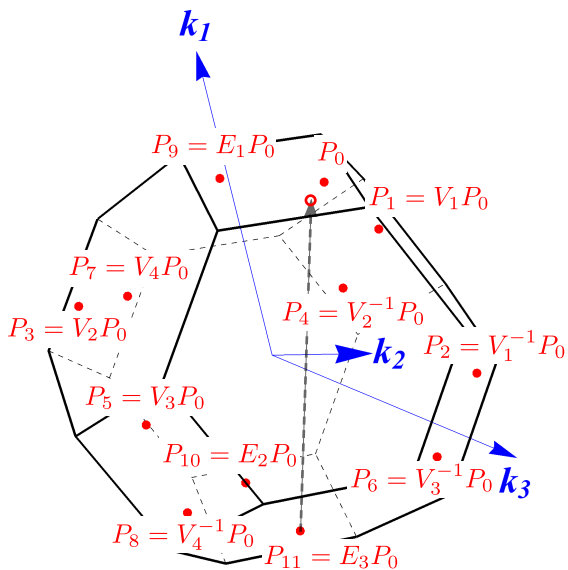


FIG. 5. Symmetric operations of the tetrahedral symmetry in the fcc Brillouin zone. The 12 points P_i ($i = 0, 1, \dots, 11$) correspond to the generated Weyl points. A dashed vector is a guide to show that a pair of the Weyl points created on the zone boundary are actually identical.

$E_3(1, 2, 3, 4) = (4, 3, 2, 1)$. Then, if we have a Weyl point with a specific chirality at a *generic point* in the Brillouin zone, S_4 generates 24 Weyl points in total. Among the 24, 12 generated by A_4 have the same chirality as the original one, while the other 12 generated by the operations involving the mirror operation have the opposite chirality as the original one. In contrast, a Weyl point on the *high symmetric X-W lines* relocate to 12 (instead of 24) points by the permutation.

B. Anisotropic case

In the previous paragraph, we have seen that the number of the Weyl points are restricted by the tetrahedral symmetry. Here, let us introduce anisotropy to break this symmetry. In the isotropic case discussed so far, we have been using $\eta'/\eta = 0.8$ for all the NNN springs. In order to induce anisotropy, we modify η'/η for the springs along $\mathbf{R}_1^{(1)}$ direction to 1. The system does not have tetrahedral symmetry anymore, but again, it should be noted that the forces on a single mass point cancel out in a pairwise manner in equilibrium, and therefore, the applied modification is not harmful in keeping the ideal diamond structure. Figure 6 shows Weyl points for the anisotropic case. Due to the symmetry breaking, timing of the creation and the annihilation differs from the isotropic case. As we decrease η , two pairs of Weyl points are generated in $k_1 = \pm\pi$ plane at $\eta = 0.81$. Then, other four pairs emerge at $\eta = 0.79$. (Remember that in the isotropic case, the six pairs are created simultaneously.)

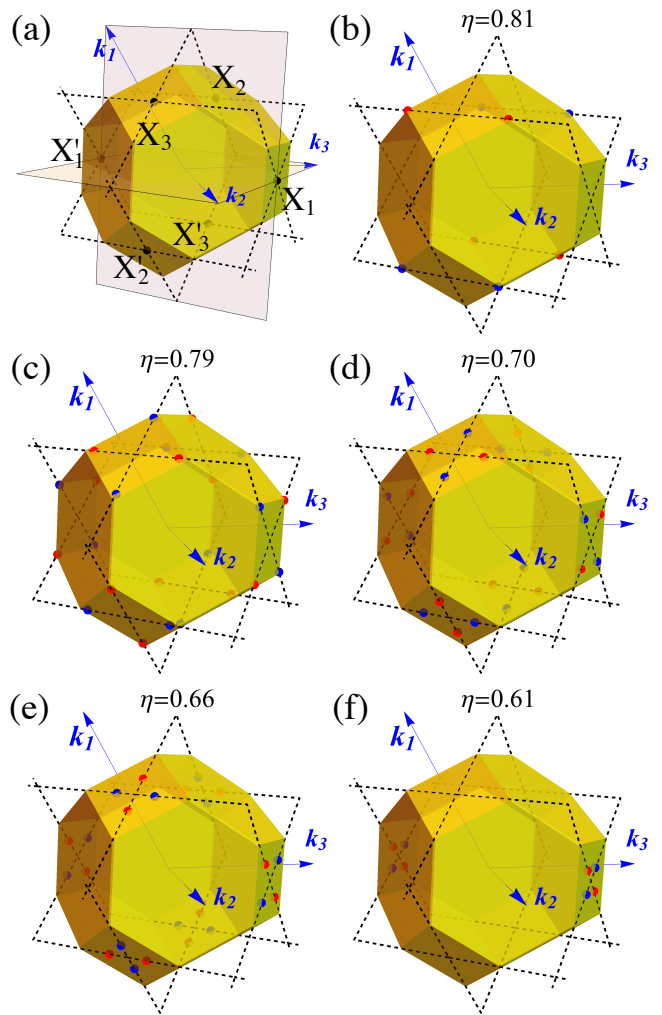


FIG. 6. (a) Notations for the high symmetric points in the Brillouin zone. X_i and X'_i ($i = 1, 2, 3$) points are equivalent respectively. The two planes indicate mirror planes in the Brillouin zone remaining in the anisotropic case. (b)-(f) Weyl points for the anisotropic case. The tension parameters are (b) $\eta = 0.81$, (c) $\eta = 0.79$, (d) $\eta = 0.70$, (e) $\eta = 0.66$ and (f) $\eta = 0.61$.

All six pairs switch the chirality in between $\eta = 0.70$ and $\eta = 0.66$, although the switch does not take place simultaneously. The switch of the four pairs near X_2, X'_2, X_3 and X'_3 points is first and that of the two pairs near X_1 and X'_1 points is second. Finally, only two pairs near the X_1 and X'_1 points remain for $\eta = 0.61$.

As we have seen, in the isotropic case, if a Weyl point is generated on X-W lines, the symmetry automatically gives 12 Weyl points in total. In the anisotropic case, the multiplicity of the Weyl points obeys a different rule. The anisotropy reduces the symmetry from A_4 to C_2 , and even if it is combined with the mirror operation, a Weyl point at a generic point is copied onto only 4 points. (Note that 4 is the expected minimum number of Weyl points with the time-reversal symmetry.) Indeed, we find

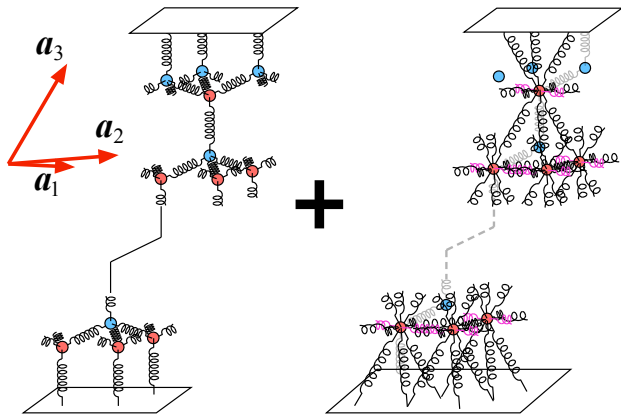


FIG. 7. Schematic picture of the NNN system with a boundary. The tension parameter for the magenta springs, which are arranged to be parallel to the surface, is different from the one for five other NNN springs.

4 Weyl points for $\eta = 0.81$, and another 8 Weyl points are added afterward as η decreases to 0.79, and so on. The key is that the symmetry breaking reduces the number of simultaneously created pairs, in consistent with the group theory.

V. BULK SECTION CHERN NUMBER AND FERMI ARC

In this section, we show chiral edge states (or Fermi arc in this case) characterized by a bulk topological number. Let us start with the definition of the bulk topological number. In our 3D model, we have section Chern number (SCN)^{35–38}, whose definition is

$$C(k_i) = -\frac{i}{2\pi} \int_S \text{Tr} d\mathcal{A} \Big|_{k_i:\text{fixed}}. \quad (10)$$

Here, \mathcal{A} is a non-Abelian Berry connection $\mathcal{A} = \psi^\dagger d\psi$. The state ψ is a triplet formed by three eigenstates with lower frequencies. The integration is taken over the two-dimensional Brillouin zone with k_i ($i = 1, 2, 3$) fixed. In the isotropic case, the SCN defined in this way is always trivial for any fixed momentum because of mirror planes passing through the k_1 -, k_2 -, and k_3 -axes. In the anisotropic model, on the other hand, $C(k_2)$ and $C(k_3)$ can be nontrivial in a certain range of fixed momentum due to the absence of a mirror plane through the k_2 - and k_3 -axes. This nontrivial SCN is related to the surface states on the specific surface in Fig. 7. Actually, the SCN can be defined on different types of 2D slices of the 3D Brillouin zone. For instance, it is in principle possible to prepare the SCN isolating the Weyl points in the isotropic case.

To obtain surface states, we consider a system that is periodic in \mathbf{a}_1 and \mathbf{a}_2 direction but finite in \mathbf{a}_3 direction. In the \mathbf{a}_3 direction, the system is terminated with the

fixed boundary condition as illustrated in Fig. 7. (When we are hanging the entire system in a cage, this corresponds to set one face of the cage along \mathbf{a}_1 - \mathbf{a}_2 plane, and focus on the motion of the mass points near that face.) The surface states with this boundary condition for the NN model has been discussed in our previous paper²⁹. Now for the NNN model, Fig. 8 shows $C(k_2)$ and surface states of a system with 400 layers in z direction for $\eta = 0.61$. As expected, we see chiral edge states connecting the third and the fourth lowest bands for k_2 with finite $C(k_2)$. $C(k_2)$ changes when the plane of fixed k_2 crosses a gapless point with topological charge, i.e., Weyl point. One monopole (antimonopole) adds +1 (−1) to the SCN. We also notice that the number of the chiral edge states matches to the SCN, with the sign of the SCN related to the sign of the slope of the chiral edge states. Note that flat bands that is already found in the NN model²⁹ remain even in the NNN model. The Fermi arc is shown in Fig. 8(i), which has no dependence on wave number in the \mathbf{k}_1 direction here.

VI. CONCLUDING REMARKS

To summarize, we have investigated Weyl points of the mechanical diamond. By introducing the NNN springs and the variation in the mass parameter, several pairs of the Weyl points in the frequency dispersion appear in the Brillouin zone. The Weyl point positions are numerically obtained by calculating topological charges. As a function of the tension parameter, the configuration of the Weyl points in the Brillouin zone shows an interesting evolution. For the isotropic case with tetrahedral symmetry, six pairs of the Weyl points move on the high-symmetric W-X lines as the tension increases. In a narrow range of the tension parameter, several extra pairs of Weyl points are created and annihilated, and after the annihilation, the chirality of the remaining Weyl points is flipped. For the anisotropic case without tetrahedral symmetry, the sequence of the creation/annihilation of Weyl points is a little different from the one in the isotropic case. We also demonstrate the relation between the surface states and the bulk SCN in the case with anisotropy.

In a practical view point, there is still a room to improve our design. For instance, the frequency-momentum range where the Fermi arcs are clearly visible is narrow in our design. It is an interesting future task to propose an elaborated design to have Weyl points better isolated from the other part of the band. Alternatively, one may elaborate the experimental observation scheme to access the narrow range in the frequency-momentum space. In a two-dimensional mechanical system with nontrivial topology, the topological edge modes are excited, for instance, by poking a mass point by air emitted by a nozzle³⁹. In principle, it is possible to improve the selectivity of the excited mode by using multiple nozzles and poking several mass points with appropriate phase shifts.

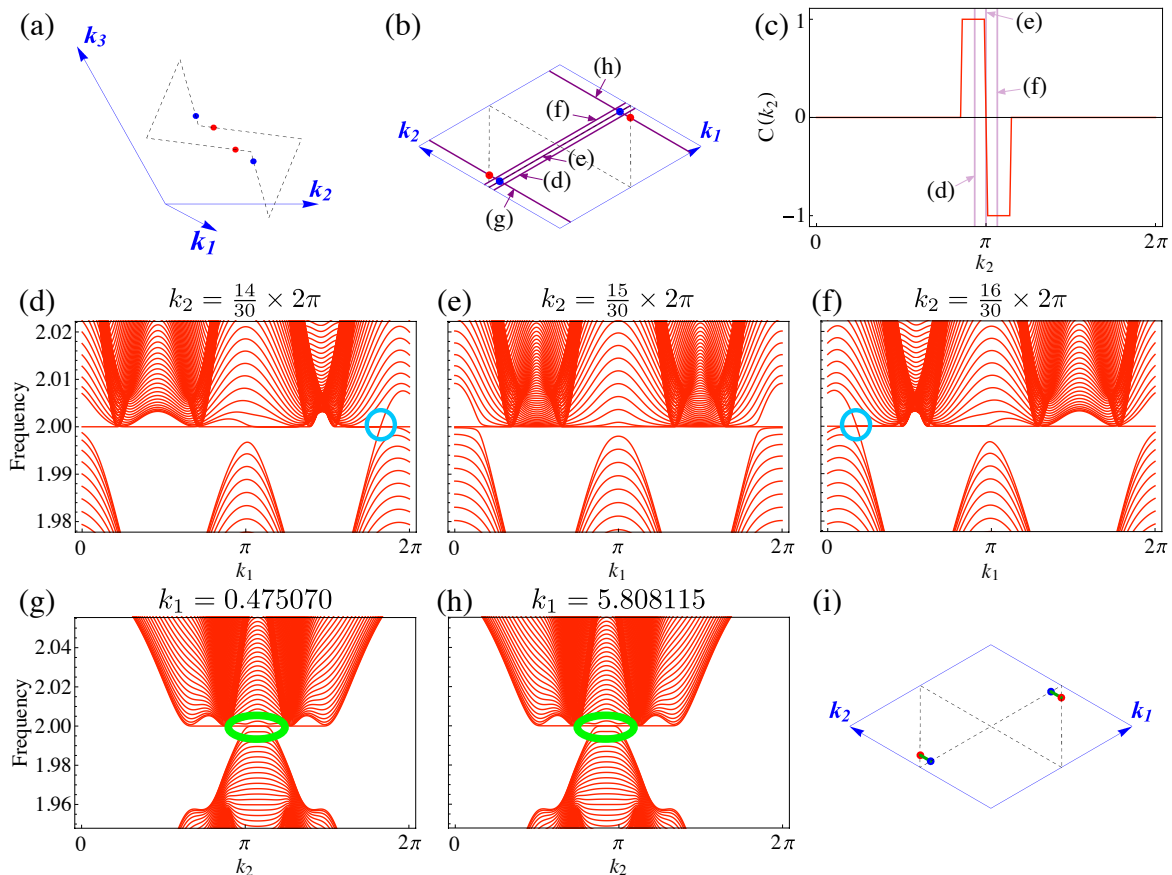


FIG. 8. (a) Weyl points of the anisotropic model for $\eta = 0.61$ in the parallelepiped Brillouin zone. (b) Weyl points projected onto the k_1 - k_2 plane. (c) SCN of this model in k_2 direction. (d)-(h) Surface band structures along the five purple lines named (d)-(h) in (b), respectively. In (d)-(f), k_2 is fixed to (d) $k_2 = \frac{14}{30} \times 2\pi$, (e) $k_2 = \frac{15}{30} \times 2\pi$ and (f) $k_2 = \frac{16}{30} \times 2\pi$, and the band structures are scanned by k_1 . In the region highlighted by an aqua circle, we see dispersive and flat bands. The dispersive one connecting the lower and the upper bands is the chiral edge mode. The flat one has also the surface origin. In (g) and (h), k_1 is fixed to (g) $k_1 = 0.475070$ and (h) $k_1 = 5.808115$, and the band structures are scanned by k_2 . (The values of k_1 are numerically determined to hit the projected Weyl points.) A Fermi arc is marked by the yellow-green ovals. (i) A Fermi arc projected onto the k_1 - k_2 plane, drawn as green lines.

Finally, it is worth noting that the current 3D printing technique might be useful for fabricating 3D structures. In a recent theoretical paper⁴⁰, the usage of the 3D printer to realize Weyl points in a vibration spectrum in an elastic media is discussed. Notably, in Ref. 40, the Weyl points are first discussed in a tight-binding model, i.e., a discrete model, which can be exactly mapped to a spring-mass model, and then propose a design of a continuum elastic system, which is 3D printable and has a vibration spectrum similar to the one in a discrete model. Although the design in our proposal and the one in Ref. 40 are very different, it opens an interesting possibility to print a system capturing essential features of

our model. One might think that the parameter η in our analysis is specific to the spring-mass model. However, as is pointed out in Ref. 28, η actually controls the ratio between the longitudinal and the transverse coupling constants, and it is likely that a clever structural design can account for that.

ACKNOWLEDGMENTS

We thank C. Mudry for useful discussions. This work was partly supported by JSPS KAKENHI Grant Numbers JP17K14358 (TK), JP16K13845 (YH), JP17H06138 and JP25107005 (YT, YH).

* takahashi@rhodia.ph.tsukuba.ac.jp

† kariyado.toshikaze@nims.go.jp

- [‡] hatsugai.yasuhiro.ge@u.tsukuba.ac.jp
- ¹ S. M. Young, S. Zaheer, J. C. Y. Teo, C. L. Kane, E. J. Mele, and A. M. Rappe, *Phys. Rev. Lett.* **108**, 140405 (2012).
 - ² Z. Wang, Y. Sun, X.-Q. Chen, C. Franchini, G. Xu, H. Weng, X. Dai, and Z. Fang, *Phys. Rev. B* **85**, 195320 (2012).
 - ³ Z. K. Liu, B. Zhou, Y. Zhang, Z. J. Wang, H. M. Weng, D. Prabhakaran, S.-K. Mo, Z. X. Shen, Z. Fang, X. Dai, Z. Hussain, and Y. L. Chen, *Science* **343**, 864 (2014).
 - ⁴ A. A. Burkov, M. D. Hook, and L. Balents, *Phys. Rev. B* **84**, 235126 (2011).
 - ⁵ S. Kobayashi, Y. Yamakawa, A. Yamakage, T. Inohara, Y. Okamoto, and Y. Tanaka, *Phys. Rev. B* **95**, 245208 (2017).
 - ⁶ Z. Yan, R. Bi, H. Shen, L. Lu, S.-C. Zhang, and Z. Wang, *Phys. Rev. B* **96**, 041103 (2017).
 - ⁷ G. Bian, T.-R. Chang, R. Sankar, S.-Y. Xu, H. Zheng, T. Neupert, C.-K. Chiu, S.-M. Huang, G. Chang, I. Belopolski, D. S. Sanchez, M. Neupane, N. Alidoust, C. Liu, B. Wang, C.-C. Lee, H.-T. Jeng, C. Zhang, Z. Yuan, S. Jia, A. Bansil, F. Chou, H. Lin, and M. Z. Hasan, *Nat. Commun.* **7**, 10556 (2016).
 - ⁸ S. Murakami, *New J. Phys.* **9**, 356 (2007).
 - ⁹ A. A. Burkov and L. Balents, *Phys. Rev. Lett.* **107**, 127205 (2011).
 - ¹⁰ C. Fang, M. J. Gilbert, X. Dai, and B. A. Bernevig, *Phys. Rev. Lett.* **108**, 266802 (2012).
 - ¹¹ A. A. Soluyanov, D. Gresch, Z. Wang, Q. Wu, M. Troyer, X. Dai, and B. A. Bernevig, *Nature* **527**, 495 (2015).
 - ¹² R. Okugawa and S. Murakami, *Phys. Rev. B* **96**, 115201 (2017).
 - ¹³ L. Lu, Z. Wang, D. Ye, L. Ran, L. Fu, J. D. Joannopoulos, and M. Soljačić, *Science* **349**, 622 (2015).
 - ¹⁴ X. Wan, A. M. Turner, A. Vishwanath, and S. Y. Savrasov, *Phys. Rev. B* **83**, 205101 (2011).
 - ¹⁵ S.-Y. Xu, C. Liu, S. K. Kushwaha, R. Sankar, J. W. Krizan, I. Belopolski, M. Neupane, G. Bian, N. Alidoust, T.-R. Chang, H.-T. Jeng, C.-Y. Huang, W.-F. Tsai, H. Lin, P. P. Shibayev, F.-C. Chou, R. J. Cava, and M. Z. Hasan, *Science* **347**, 294 (2015).
 - ¹⁶ Y. Hatsugai, *Phys. Rev. Lett.* **71**, 3697 (1993).
 - ¹⁷ F. D. M. Haldane and S. Raghu, *Phys. Rev. Lett.* **100**, 013904 (2008).
 - ¹⁸ Z. Wang, Y. D. Chong, J. D. Joannopoulos, and M. Soljačić, *Phys. Rev. Lett.* **100**, 013905 (2008).
 - ¹⁹ E. Prodan and C. Prodan, *Phys. Rev. Lett.* **103**, 248101 (2009).
 - ²⁰ C. L. Kane and T. C. Lubensky, *Nat. Phys.* **10**, 39 (2014).
 - ²¹ H. C. Po, Y. Bahri, and A. Vishwanath, *Phys. Rev. B* **93**, 205158 (2016).
 - ²² J. Paulose, B. G.-g. Chen, and V. Vitelli, *Nat. Phys.* **11**, 153 (2015).
 - ²³ D. Z. Rocklin, B. G.-g. Chen, M. Falk, V. Vitelli, and T. C. Lubensky, *Phys. Rev. Lett.* **116**, 135503 (2016).
 - ²⁴ P. Wang, L. Lu, and K. Bertoldi, *Phys. Rev. Lett.* **115**, 104302 (2015).
 - ²⁵ J. E. S. Socolar, T. C. Lubensky, and C. L. Kane, *New J. Phys.* **19**, 025003 (2017).
 - ²⁶ J. Cserti and G. Tichy, *Eur. J. Phys.* **25**, 723 (2004).
 - ²⁷ Y.-T. Wang, P.-G. Luan, and S. Zhang, *New J. Phys.* **17**, 073031 (2015).
 - ²⁸ T. Kariyado and Y. Hatsugai, *Sci. Rep.* **5**, 18107 (2015).
 - ²⁹ Y. Takahashi, T. Kariyado, and Y. Hatsugai, *New J. Phys.* **19**, 035003 (2017).
 - ³⁰ E. I. Blount, *Phys. Rev. B* **32**, 2935 (1985).
 - ³¹ In our design, the forces exerted by the springs are balanced between themselves, but if we further consider the gravity, we may have to add extra springs to compensate it.
 - ³² T. Fukui, Y. Hatsugai, and H. Suzuki, *J. Phys. Soc. Jpn.* **74**, 1674 (2005).
 - ³³ M. Hirayama, R. Okugawa, and S. Murakami, arXiv:1708.05791.
 - ³⁴ The transition occurs very close to 2/3, but we can shift this value by changing parameters in our model without breaking symmetry, and 2/3 is unlikely to be a special value.
 - ³⁵ J. E. Avron, R. Seiler, and B. Simon, *Phys. Rev. Lett.* **51**, 51 (1983).
 - ³⁶ B. I. Halperin, *Jpn. J. Appl. Phys.* **26**, 1913 (1987).
 - ³⁷ M. Kohmoto, B. I. Halperin, and Y.-S. Wu, *Phys. Rev. B* **45**, 13488 (1992).
 - ³⁸ Y. Hatsugai, S. Ryu, and M. Kohmoto, *Phys. Rev. B* **70**, 054502 (2004).
 - ³⁹ L. M. Nash, D. Kleckner, A. Read, V. Vitelli, A. M. Turner, and W. T. M. Irvine, *Proc. Natl. Acad. Sci.* **112**, 14495 (2015).
 - ⁴⁰ Y.-T. Wang and Y.-W. Tsai, *New J. Phys.* **20**, 083031 (2018).